



THE UNIVERSITY *of* EDINBURGH

## Edinburgh Research Explorer

# Implementing an Insect Brain Computational Circuit Using III–V Nanowire Components in a Single Shared Waveguide Optical Network

### Citation for published version:

Winge, DO, Limpert, S, Linke, H, Borgström, MT, Webb, B, Heinze, S & Mikkelsen, A 2020, 'Implementing an Insect Brain Computational Circuit Using III–V Nanowire Components in a Single Shared Waveguide Optical Network', *ACS Photonics*, vol. 7, no. 10, pp. 2787-2798.  
<https://doi.org/10.1021/acsp Photonics.0c01003>

### Digital Object Identifier (DOI):

[10.1021/acsp Photonics.0c01003](https://doi.org/10.1021/acsp Photonics.0c01003)

### Link:

[Link to publication record in Edinburgh Research Explorer](#)

### Document Version:

Publisher's PDF, also known as Version of record

### Published In:

ACS Photonics

### General rights

Copyright for the publications made accessible via the Edinburgh Research Explorer is retained by the author(s) and / or other copyright owners and it is a condition of accessing these publications that users recognise and abide by the legal requirements associated with these rights.

### Take down policy

The University of Edinburgh has made every reasonable effort to ensure that Edinburgh Research Explorer content complies with UK legislation. If you believe that the public display of this file breaches copyright please contact [openaccess@ed.ac.uk](mailto:openaccess@ed.ac.uk) providing details, and we will remove access to the work immediately and investigate your claim.



# Implementing an Insect Brain Computational Circuit Using III–V Nanowire Components in a Single Shared Waveguide Optical Network

David O. Winge,\* Steven Limpert, Heiner Linke, Magnus T. Borgström, Barbara Webb, Stanley Heinze, and Anders Mikkelsen\*



Cite This: *ACS Photonics* 2020, 7, 2787–2798



Read Online

ACCESS |



Metrics & More



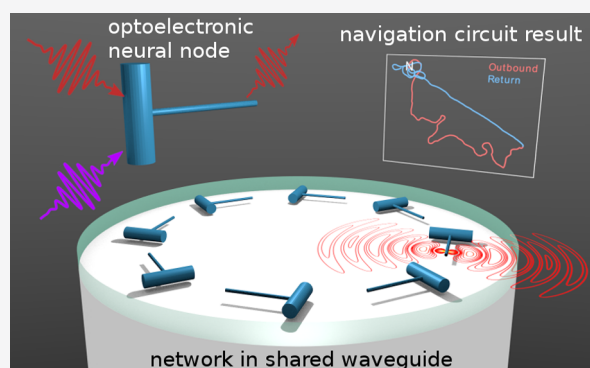
Article Recommendations



Supporting Information

**ABSTRACT:** Recent developments in photonics include efficient nanoscale optoelectronic components and novel methods for subwavelength light manipulation. Here, we explore the potential offered by such devices as a substrate for neuromorphic computing. We propose an artificial neural network in which the weighted connectivity between nodes is achieved by emitting and receiving overlapping light signals inside a shared quasi 2D waveguide. This decreases the circuit footprint by at least an order of magnitude compared to existing optical solutions. The reception, evaluation, and emission of the optical signals are performed by neuron-like nodes constructed from known, highly efficient III–V nanowire optoelectronics. This minimizes power consumption of the network. To demonstrate the concept, we build a computational model based on an anatomically correct, functioning model of the central-complex navigation circuit of the insect brain. We simulate in detail the optical and electronic parts required to reproduce the connectivity of the central part of this network using previously experimentally derived parameters. The results are used as input in the full model, and we demonstrate that the functionality is preserved. Our approach points to a general method for drastically reducing the footprint and improving power efficiency of optoelectronic neural networks, leveraging the superior speed and energy efficiency of light as a carrier of information.

**KEYWORDS:** nanowire, neural network, phototransistor, optoelectronic modeling, optoelectronic device, optical interconnects, insect brain, polarization anisotropy



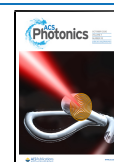
The neural computation performed by real brains remains an important inspiration for machine intelligence. However, software implementations of artificial neural networks using standard computer hardware are orders of magnitude less energy efficient compared to biological brains,<sup>1,2</sup> limiting future applications. To address this challenge, a multitude of physical/chemical mechanisms such as memristors,<sup>3</sup> ionic liquids,<sup>4</sup> and spintronics<sup>5</sup> are being explored to realize naturalistic neural networks.<sup>6</sup> Recently, the use of photonics-based solutions has gained renewed interest,<sup>7–9</sup> as it can overcome both speed and efficiency limits of standard technology for neural networks.<sup>7,10–13</sup> For bioinspired processing networks, a main energy expenditure and complexity challenge is in the need for a large number of communication connections between components.<sup>10,14</sup> Using light for network connectivity is, in principle, a superior solution, as it can transmit information quickly and with high energy efficiency. However, realizing the full potential of optical solutions is hindered by their large circuit footprint and the energy losses in regular (macroscopic) optoelectronic components. Even in recent work on (impressive) integrated

optical network solutions, the circuit footprint is many hundreds of microns across.<sup>9,10</sup> The plethora of recently developed nanoscale photonic components, such as semiconductor nanowires, present an avenue to solving these challenges, which has not yet been explored.

Significant progress has been made in concentrating and manipulating light using nanostructure components, thus, allowing for the necessary miniaturization of optical computation circuitry. In particular, III–V nanowires have matured into a versatile, controllable, and well-characterized nanotechnology platform. This has allowed the development of novel light harvesting<sup>15–17</sup> and emission technologies,<sup>18–20</sup> as well as combining with Si-based technology.<sup>21</sup> III–V

Received: June 22, 2020

Published: September 23, 2020



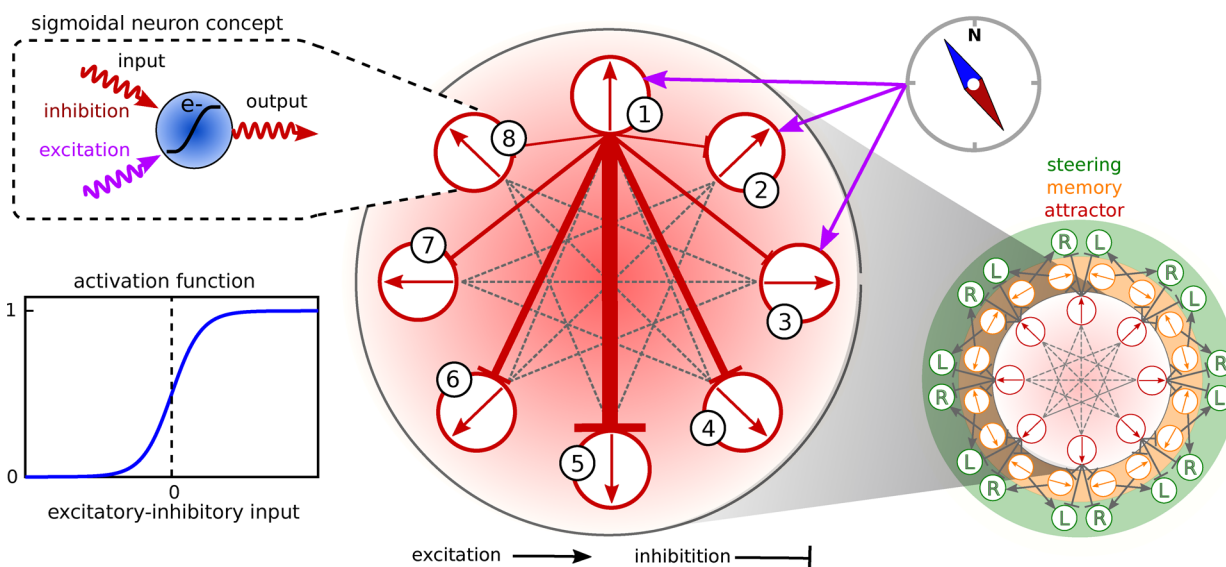


**Figure 1.** Ring-attractor network that is implemented in this study. It is the most connected subcircuit of the insect brain central complex model (CX) of Stone et al.<sup>34</sup> The CX neural network main parts (schematically shown in bottom right) can be represented in a circular topology as three concentric and interconnected ring network layers (attractor, memory, and steering). The ring-attractor layer (focus of present study) is shown in the center of Figure 1. The eight neural nodes (neurons) in the ring attractor are shown as circles, with arrows representing a 2D heading of the insect. All attractor neurons are mutually inhibiting and simultaneously provide (inhibiting) signal information to the outer network layers. For clarity, only the inhibiting connections from node 1 to the other nodes are shown (red lines) in the central part of Figure 1. The weights are given by the thickness of the lines. The existence of the other interconnections is indicated as dashed gray lines. The input to each node is given by external compass neurons, as exemplified by the purple arrows. The schematics of the sigmoid neural node are shown in the top left corner. It receives inhibiting/exciting signals and outputs either an inhibiting or exciting signal. Inset in bottom left corner exemplifies the sigmoidal electronic data processing of each neural node.

heterostructure nanowires can uniquely be tailored with widely varying optical and electronic properties. They respond locally and efficiently to optical signals, concentrate light on a subwavelength scale,<sup>22,23</sup> and have a natural polarization sensitivity<sup>24</sup> that has been used for optical logical gates.<sup>25</sup> Importantly, they can have a much higher absorption cross-section than their physical size<sup>22,23</sup> and can thus act as efficient photodetectors. Precise and varied large-scale 2D arrays of functionalized nanowires<sup>22</sup> and single nanowire optical emitters with controllable emission patterns,<sup>19,20,26,27</sup> as summarized by Mantynen et al.,<sup>28</sup> have been manufactured and experimentally studied in detail.

An excellent way to explore the potential of III–V nanostructured components for neural networks is to implement specific circuit models based on a detailed understanding of biological neural circuits. The insect brain offers substantial advantages as a target, as its lower complexity and higher accessibility supports the functional understanding at the single neuron level. At the same time, insects are capable of tasks well beyond the reach of current artificial neural nets, such as traveling across hundreds of kilometers of unfamiliar terrain to pinpoint a specific breeding ground,<sup>29,30</sup> or returning to a near invisible nest entrance from several kilometers away in a straight-line trajectory, after a convoluted searching trip through dense vegetation.<sup>31</sup> Using only a few drops of nectar as an energy supply, they achieve all this with a brain the size of a grain of rice, which contains about 100000× fewer neurons than mammalian brains.

One module of the insect brain conserved across species with vastly different lifestyles is the central complex (CX), which is a brain region containing core decision-making and motor-control circuits.<sup>32,33</sup> The neural circuit of the CX has been decoded in great detail, which is of the utmost

importance to any attempt to mimic the neural functionality. It is characterized by tight structure–function coupling, in which the anatomical layout of a circuit defines its computations. One important purpose of this neuronal circuit is to serve as a navigational control system that underlies most planned, directed movements of insects.<sup>32</sup> The CX has been distilled to its fundamental neuroarchitecture, and the function of a number of its components was mapped onto a biologically constrained computational model.<sup>34</sup> This model has the ability to integrate the outward going path of a simulated insect leaving its nest and to switch into producing the required steering signals to enable the insect to navigate directly back to its point of origin. This homing task is successfully carried out using the input of limited precision and with considerable circuit noise. Containing less than 100 neurons of qualitatively similar function, the CX model is simple enough to serve as a target system for investigating novel nanotechnology solutions for neural networks while still being important for solving real navigational tasks in insects.

In this paper, we describe how the spatial and energy footprint of an optical neural network that reproduces a key part of the insect CX circuit can be minimized using nanocomponents placed inside a shared waveguide. We first describe the model of the CX that we implement and the general requirements of the nodes and their network intercommunication architecture. These principles should be widely applicable in reproducing any neural circuit. Second, a nanowire-based device is shown to be a prime candidate for the neural node, as it can have a very small energy consumption and large cross-section for light detection. Third, optical simulations on the network level demonstrate how the interdevice coupling weights are set by emission patterns and geometrical layout inside a shared quasi 2D

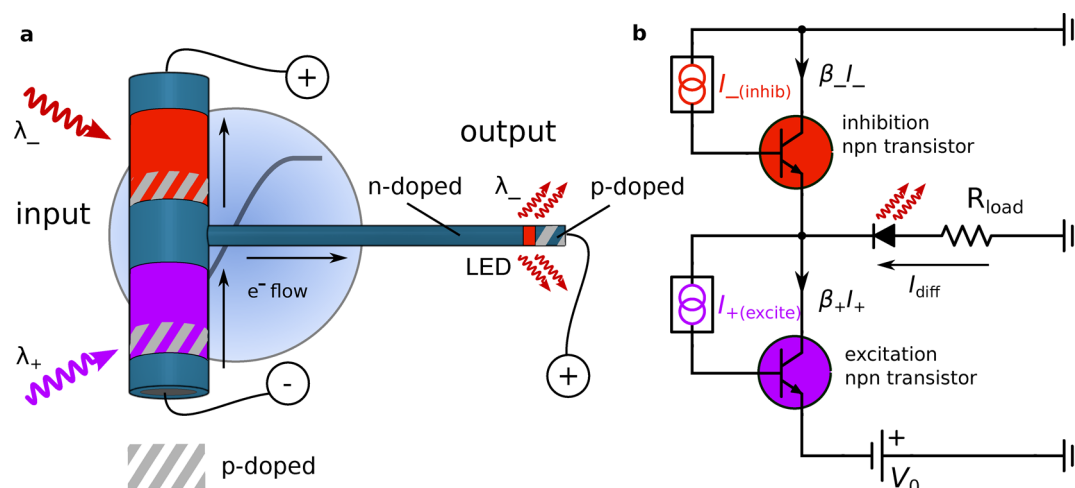


**Figure 2.** Schematics of the nanowire-based artificial neuron that will evaluate input light signals, resulting in an appropriate light output. (a) Diagram of the neural node component that is a branched nanowire with two npn transistors in the stem and a LED in the branch. The red and purple parts indicate III–V materials of a smaller bandgap than the dark blue areas around. Specific parameters are given in Table 1. p-doped regions on the nanowire are indicated by the gray stripes. All other parts of the nanowire are n-doped. Electrical contacts needed to power the component are indicated. (b) Equivalent circuit model of the component in (a) with the floating base npn phototransistors modeled with current sources representing the generated exciting and inhibiting photocurrents.

waveguide. This broadcasting strategy is a key component of our design, as it reduces the spatial footprint of the network, removing the need for both internode connecting waveguides and interdevice electrical wiring. Fourth, the results from the electrical and optical modeling are tested by substituting it into the full computational model of the insect brain CX circuit,<sup>34</sup> successfully demonstrating that the navigation capability is preserved. Finally, we evaluate the operational efficiencies needed in order to realize our optoelectronic implementation.

## RESULTS

**General Concept of the Neural Network and Its Implementation.** To establish the basic design criteria for our hardware solutions, we provide a brief discussion of the insect brain neural navigation network model of Stone et al.,<sup>34</sup> which is the foundation for exploring and demonstrating our approach. Converted into mathematical form and implemented on a standard computer, the CX network allows an insect to be guided back to its nest after a foraging trip (“the insect” in this case is an abstract agent in the computer that receives input data from either an artificial or a real environment; the model has been shown to work for a real-world robot<sup>34</sup>). The model uses the insect’s current heading and speed as input and, by integration, generates an internal (vector) representation of the angle and distance of the point of origin. Once homing is initiated, the same circuit outputs a left or right steering signal that indicates how the insect should change its heading in order to move homeward. The model can perform this task with limited, noisy input data and deals successfully with obstacles blocking its path. It can function with internal noise levels in the neural processing of up to 20%.

In the lower right corner of Figure 1, we show the three main network layers of this navigational circuit, which can be represented topologically as concentric circles. The innermost layer and the heart of the CX model is a ring-attractor circuit, which constantly keeps track of the heading of the insect. This layer receives its input from specialized compass neurons, as schematically indicated in the top right of Figure 1. Each ring-attractor neural node communicates both inward with its peers

as well as outward with the subsequent layers of the circuit. This adds a recurrent feature to this layer. The second layer is a memory layer, which receives input from both the ring-attractor and the speed-input neurons (not drawn in Figure 1). Using this information, it performs a path integration to keep track of the home direction. The third layer compares the current heading direction from the ring attractor with the desired heading toward home, given by the memory neurons, to compute the steering signal. This description summarizes features of the network relevant for the present paper; for further details and biological justification of the circuit design refer to Stone et al.<sup>34</sup>

In the present study, we focus on the innermost ring attractor layer, which has the largest and most complex connectivity pattern. The nodes in this subcircuit perform signal evaluation in a qualitatively similar fashion to all other nodes across the network. Implementing this inner ring will, therefore, demonstrate and test the main aspects of our approach. This requires the design of an optoelectronic component that can serve as a node as well as designing a network of these nodes that fulfils the interconnection weight requirements.

The artificial neuron (neural node component) to be constructed is a sigmoidal neuron entity, as schematically shown in the top left inset of Figure 1. Sigmoidal neurons operate using a rate code, that is, the frequency of neuronal action potentials is encoded as a continuous numerical value. This generic neuron type will receive external inhibiting and exciting input from multiple sources. It may also have an internal input source (for example, a bias) that creates an offset in the activation function. All inputs are weighed, added, and the sum evaluated via a nonlinear sigmoidal function, which will result in activation of an output signal (if the excitation sufficiently dominates inhibition) that must then be transferred to several other neurons. For biologically inspired neural implementations of the node, it is important that both the slope and the offset of the activation function can be tuned. In our hardware implementation, the neural firing rates of both input and output signals are represented by light intensities



(rate of photons), while the sigmoid evaluation is performed electrically within each neural node component.

A topological illustration of the ring attractor is provided in the center of Figure 1. Each of the eight neurons in the ring attractor network are represented by a circle with an arrow that, in turn, represents a specific directional heading of the insect. In the specific CX architecture, exciting inputs provide compass and speed information, while the neurons communicate via inhibiting signals among themselves. The strongest inhibition is from the neural node on the opposite side of the ring, gradually falling off for neighboring nodes. This stabilizes the activity in the inner ring to a single bump centered on one of the neurons.<sup>34</sup> This is how the insect obtains a robust sense of direction.

To achieve this weighted communication, the neural-node components will be distributed within a single planar waveguide in a circular pattern (resembling the topological layout of the circuit, see Figure 1), and the light emission patterns of the nodes will be shaped using the morphology of the nano-optoelectronic/photonic structures. As the communication between the neural nodes is achieved inside a single shared waveguide, the inhibiting and exciting signals must operate alongside at different wavelengths. The multitude of collected signals in each node represent a clear analogy to the dendrites of biological neurons. The waveguide defines the plane of computation: each node responds to all available local optical signals and emits the appropriate nonlinear response into the waveguide anew. This approach allows us to use the propagation direction normal to the waveguide plane for supplying input signals as well as for probing of the network.

**Sigmoidal Neural Node Component.** In this section we propose a specific III–V nanowire-based implementation of the sigmoidal neuron and present simulations demonstrating that it meets the biologically defined functional criteria,<sup>34</sup> as also discussed above. In brief, this component should receive (inhibiting and exciting) optical signals, weight and sum them, process the results through a sigmoid activation function (with variable slope/offset), and broadcast an optical (inhibiting or exciting) signal. The T-shaped component that performs these tasks is shown in Figure 2. To be practically feasible, the design is made as simple as possible and is based on existing types of III–V nanostructures. It consists of a nanowire stem with two npn heterojunction bipolar phototransistors (for input) and a nanowire branch with an LED (for output). Specific values for component dimensions and material compositions are given in Table 1.

The two colored regions (purple/red) in Figure 2a indicate materials with bandgaps corresponding to the wavelengths of the excitation ( $\lambda_+$ ) and inhibition light signals ( $\lambda_-$ ), respectively (we choose  $\lambda_+ < \lambda_-$ ). When light signals at  $\lambda_+$  generate a photocurrent ( $I_+$ ), the excitation phototransistor opens up, resulting in a current ( $\beta_+ I_+$ ) to the LED, if no inhibition signal is present ( $\beta_+$  is the current gain of the respective transistors). When a  $\lambda_-$  light signal is present, this generates a photocurrent ( $I_-$ ) and the inhibition phototransistor opens. As a result, part of the current  $\beta_+ I_+$  flows to the ground as  $\beta_- I_-$  instead of exciting the LED. We note that the material region absorbing at  $\lambda_-$  is susceptible also to the excitatory  $\lambda_+$  signal (because  $\lambda_+ < \lambda_-$ ). To avoid significant signal contamination, experimentally verified wavelength and polarization-specific nanoantennas<sup>35</sup> can be used to focus the external excitatory light input on the  $\lambda_+$  region (signal transmission is discussed more in the next section). The

**Table 1. Neural Node Component Materials and Parameters<sup>a</sup>**

parameter	value	excitation	inhibition
$D_{\text{stem}}$	200 nm		
$L_{\text{stem}}$	700 nm		
$D_{\text{branch}}$	50 nm		
$L_{\text{branch}}$	1000 nm		
LED QW	InP		
$\lambda$		750 nm	830 nm
$\beta$		1400	1900
emitter		$\text{Al}_{0.4}\text{In}_{0.6}\text{P}$	$\text{Al}_{0.3}\text{In}_{0.7}\text{P}$
base/collector		$\text{Al}_{0.1}\text{In}_{0.9}\text{P}$	InP
other sections	$\text{Al}_{0.3}\text{In}_{0.7}\text{P}$		

<sup>a</sup>For the excitation and inhibition photo-transistors the respective materials parameters are given. The wavelength  $\lambda$  is the target wavelength that matches the respective bandgap and  $\beta$  is current forward gain (based on detailed modeling, as described in the SI). In Figure 2a, the base and collector are colored red and purple for inhibition and excitation light signal absorption regions, respectively.

external resistance in series with the LED in Figure 2b is designed to be large enough to cause saturation above a certain current  $I_{\text{sat}}$  as discussed in Methods. The ideal mathematical function for the current across the LED can then be expressed as

$$I_{\text{diff}} = \min(I_{\text{sat}}, (\beta_+ + 1)I_+ - (\beta_- + 1)I_-), \quad \beta_+ I_+ > \beta_- I_- \geq 0 \quad (1)$$

which constitutes a basic nonlinear activation function. The inequality (noted with eq 1) arises as the current through the inhibition phototransistor cannot exceed the current through the excitation phototransistor.

An equivalent circuit diagram of the component is shown in Figure 2b, which is used to separate the detailed modeling into three (inhibiting, exciting, and emitting) nanowire subcomponents. Using physical models, with parameters extracted from experimental studies, we simulate the behavior of these three individual subcomponents. By mapping the results onto the equivalent circuit elements in Figure 2b, the complete neural node is modeled to demonstrate the required functionality. The more realistic simulation results in deviations from the ideal mathematical function, which is included in the evaluation of the neural processing capabilities and used in the detailed component design.

The detailed design should be experimentally realizable using well-known techniques for heterostructure nanowire growth and selective doping along the principal axis (as will be discussed in more detail below). In Figure 3, the main results from modeling the node component are presented. Figure 3a shows a band diagram for the inhibiting phototransistor section of the T-component stem in a floating base configuration. The emitter, base, and collector regions (E, B, and C) are created by selective p- and n-doping. The smaller bandgap region, from  $x \sim 100$  to  $\sim 300$  nm, effectively leads to an accumulation of the photogenerated holes in the base, while the electrons are separated out by the base-collector *pn*-junction. The holes eventually recombine with electrons diffusing into the base. This process is dominated by nonradiative processes and counteracts the accumulation of holes and leads to a steady state for a given intensity. A larger bandgap material has been chosen for the emitters (see Table 1) to avoid undesired excitation by the light input signals. The

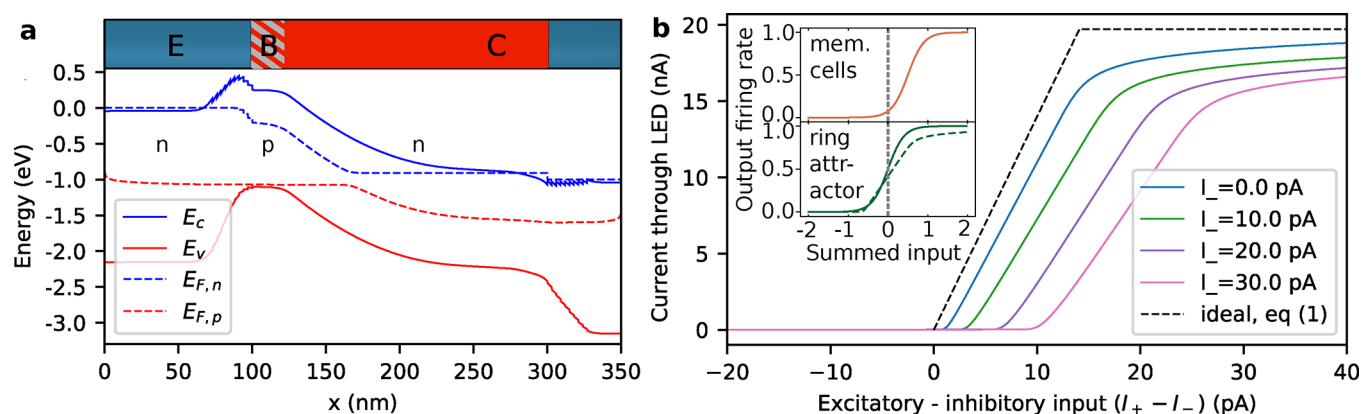


**Figure 3.** Results from the electronic modeling of the III-V neural node component in Figure 2. (a) Band diagram of the inhibiting npn phototransistor at an applied bias of 1 V. Above the diagram the nanowire stem regions of larger (blue) and smaller (red) band gap are shown as well as the differently doped emitter, base and collector regions (marked E, B, and C). This corresponds to the top half of the stem seen in Figure 2a. Solid lines represent band edges and dashed lines quasi-Fermi levels. (b) Results from modeling the full circuit in Figure 2b with the parameters  $V_0 = 3.0$  V and  $R_{\text{load}} = 30$  M $\Omega$ . Current through the LED as a function of the difference in exciting and inhibiting currents for different fixed values of inhibiting currents is shown. For comparison, eq 1 is also shown as a dashed line. Inset shows two different activation functions from Stone et al.<sup>34</sup> Dashed line in ring attractor inset shows the renormalized nanowire node component activation function for comparison.

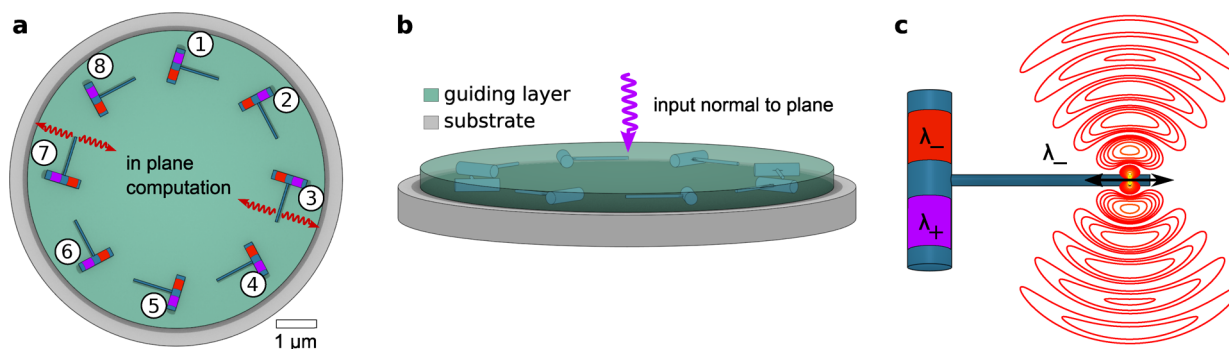


**Figure 4.** Drawing of the inner ring attractor network using the neural node component shown in Figure 2. (a, b) Top and side view of the network, encapsulated in a SiO<sub>2</sub> substrate/HfO<sub>2</sub>/air 2D waveguide. Scale bar is given in (a). The internal inhibiting signaling at  $\lambda_-$  between neural nodes occurs in the 2D plane of the network system as seen in (a). The external exciting light (compass) input at  $\lambda_+$  enters perpendicular to the 2D communication plane, as seen in (b). To ensure that the exciting signals reach the correct input position, nanoantennas<sup>35</sup> can be used. (c) One node with the superimposed emission pattern of a dipole source. The two absorption regions are again indicated by red/purple, as in Figure 2.

exciting npn phototransistor behaves in a qualitatively similar fashion as the inhibiting and is discussed in the [Supporting Information \(SI\)](#). The LED branch is designed in the same material system as the phototransistors, with a *pn*-junction defined by selective doping along the principal axis of the branch. In the center of the junction, an undoped emission section with a smaller bandgap (than the adjacent Al<sub>0.3</sub>In<sub>0.7</sub>P sections) is placed in order to increase the spatial overlap of holes and electrons, maximizing efficiency. In the present case, the material in the emission section will be InP, as we want the component to output a signal at the inhibiting wavelength  $\lambda_-$ . For a detailed description of the phototransistor, LED design, and modeling, see [Methods](#) and the [SI](#).

In Figure 3b, the current through the LED as a function of combined excitation and inhibition is shown, exemplifying the results from the modeling of the complete T-component. The inset displays two examples of activation functions used by neurons of the full network model.<sup>34</sup> They are characterized by their slope and offset (inversion point), which varies for different types of neurons. The proposed neural node component can reproduce these varying functional features. The slope depends both on the bias over the component as well as on the design parameters, such as base region length,

emitter-base bandgap offset, and doping.<sup>36</sup> The saturation current can be directly controlled by the load resistance (see the [SI](#) for examples). As seen in the inset of Figure 3b, the node component naturally produces a result similar to the activation function of the memory layer neurons of Stone et al.<sup>34</sup> A zero point offset must be added to replicate the behavior of the ring-attractor neurons. This can be accomplished by adding a background input light at a constant level, effectively expressing the signal relative to this background. The total input signal would be operated at fixed duty cycle (see the [SI](#) for estimates of the component time constants). An alternative method would be to connect an additional bias point to the neural node component.

Figure 3b further shows that the onset of the activation function as well as its slope is shifted for increasing inhibiting currents. The onset shift is due to the difference in current gain  $\beta$  of the excitation and inhibition npn transistors, while the effect of a changing slope for higher inhibition currents is a consequence of the nonideal elements of the equivalent circuit model. When simulating the complete CX network function (see below), the effects were fully included and no degradation of the performance due to these effects was observed.

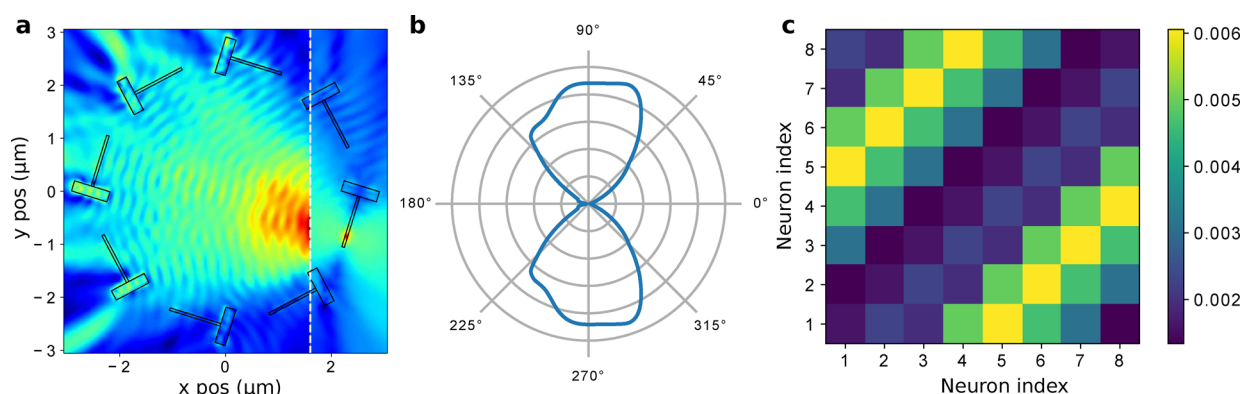


**Figure 5.** Simulated field distributions in the ring attractor network and resulting communication matrix. (a) The field distribution of dipole emission from neural node 3 (as denoted in Figure 4a) in the  $xy$ -plane of the waveguide based on FDTD modeling. To the right of the dashed white line, a log scale is used to visualize the fields close to the dipole source. (b) Polar emission pattern from the radiating dipole inside the nanowire branch (oriented horizontally in the figure). (c) Internode weight matrix calculated from the absorption in each component, with labels as in Figures 1–4. An asymmetry can be seen due to the rotation of the components, as seen in Figure 4a.

**Communication between Neural Nodes in the Ring-Attractor Network.** We now discuss the placement and emission patterns of the neural node components to achieve weighted communication via optical signals in the shared waveguide structure. As shown in Figure 4a,b, the components are positioned in a geometry directly inspired by the topographic representation of the ring-attractor central network shown in the center of Figure 1.

To obtain the desired pattern of coupling coefficients in the ring attractor (see Figure 1 and Stone et al.<sup>34</sup>), a node should emit the maximum signal toward the node farthest away in the circle, gradually decreasing toward the two closest nodes. Any self-inhibition due to the LED coupling to the phototransistors in the individual node component should be minimized. To fulfill these conditions a dipolar radiation pattern from the LED is suitable. The dipole source serves the additional purpose of transmitting signals in the 2D plane outward from the network center. This facilitates the necessary communication of the ring attractor with the nodes in the two outer ring network layers (indicated in Figure 1, bottom right).

As seen in Figure 4a, the inhibition part of the nanowire stem of each neural node faces inward, which maximizes the absorption cross-section for receiving light signals from the other nodes. The components are placed on a flat  $\text{SiO}_2$  substrate and covered with  $\text{HfO}_2$  (as depicted in Figure 4b). The  $\text{SiO}_2$  substrate/ $\text{HfO}_2$ /air structure functions as a quasi 2D waveguide. As a result, a majority of the intensity is spread in the waveguide, which is important to keep the efficiency of the network high. Nanowires have been reported to have giant polarization anisotropy.<sup>37</sup> As a result, the coupling of light from inside the nanowire to its surroundings depends on the polarization. The large dielectric contrast between the nanowire and surrounding  $\text{HfO}_2$  strongly favors coupling to light fields polarized parallel to the nanowire axis. The dipole emission pattern corresponding to this polarization is shown in Figure 4c and it determines the weights on each neural node component (along with their placement).

To quantify the absorption and emission between the components and to calculate the corresponding coupling weight matrix  $g_{ij}$ , a full 3D model of the optical network with its node components was implemented in a Finite Difference Time Domain (FDTD) simulation using the solver from Lumerical.<sup>38</sup> FDTD methods are widely used to model

nanowire optical absorption,<sup>23</sup> scattering,<sup>39</sup> and emission,<sup>19,40</sup> demonstrating good agreement with experimental observations in nanostructures as used in the present study. In Figure 5a,b, the field distributions in the attractor ring due to one neural node LED (#3 in Figure 4a), as well as from an individual component, are seen.

The absorption of each component was determined by calculating the optical transmission through a closed box around each absorption region in a component. The fraction of intensity absorbed in component (i) relative to the emitted power of component (j) directly corresponds to the weight matrix indices  $g_{ij}$  displayed in Figure 5c. The intensity flowing out of the waveguide in both the horizontal and the lateral directions was recorded to calculate the waveguide confinement factor  $\Gamma$ , found to be around 60% at 830 nm. The remaining 40% is light lost from the communication processes. Stand-alone modeling of one node component was also performed to understand how the thick receiver branch interferes with the dipole emission. The resulting intensity emission pattern  $w(\theta)$  is shown in Figure 5b, demonstrating that the main dipole shape of the radiation is retained. In the SI we discuss the dipolar emission from nanowires embedded in the waveguide structure in more detail.

Even with a dipole emitter, the absorption region of a component is subject to some radiation from its own LED, so that  $g_{ii} \neq 0$ . It is important to minimize any such reabsorption because it leads to undesirable self-inhibition in the component. For the network to perform well, it is enough that  $g_{ii}$  is substantially smaller than the internode coupling coefficients  $g_{ij}$ . This can be achieved using the polarization selectivity of the dipole source and extending the branch to move the LED away from the stem. Increasing the length of the branch, however, increases the footprint and asymmetry of the network circuit, but a sweet spot can be found that optimizes all these parameters sufficiently for excellent functionality. These considerations set the length of the LED branch used in the neural node design (given in Table 1).

The placement of the T-components (as seen in Figure 4a) results in an asymmetry of the signal reception. For example, the distances from the LED of node component 1 to nodes 4 and 6 are not identical. This leads to an overall asymmetry in the network interconnecting weights as is observed in the matrix plot in Figure 5c, which is based on the simulation



including all eight nodes. Results given in the following section show that this has no significant influence on the navigational capacity of the network.

**Simulation of the Full Navigation Network Using the III–V Nanowire-Based Ring-Attractor.** Using the complete computational model of the insect navigation CX,<sup>34</sup> the performance of the network, when realized using III–V nanowire components, was tested. The activation functions in the ring attractor (inset of Figure 3b) were replaced with the results obtained from the component response simulation (full plot in Figure 3b). In addition, the communication weights connecting the ring attractor nodes were replaced by the simulated counterparts of the matrix seen in Figure 5c. For use in the computational model, the output current (for input current see Methods), as well as the weight matrix values, were normalized to unity. Here it is important to reiterate that, while the original CX model neural node has a 1D simple sigmoidal functional response (which depends only on the difference between the sum of inhibiting and sum of exciting signal intensities), the separate values play a role in the III–V components. Thus the response function is now 2D in the intensities of the inhibiting and exciting signals. Such a 2D functional (shown in Figure S9) will be an almost inevitable consequence when constructing a real component. Only if the amplification in both transistors is identical and slope-saturation can be avoided, it would in the present case revert to the model 1D response. However, our simulations show that the more complicated response still allows full network functionality.

The results of the navigation tests are summarized in Figure 6 using the physical parameters from the III–V components placed in the network. In Figure 6a, an example route with 1500 steps is shown where the insect finds its way back without difficulty with 10% added noise. In Figure 6b, the results of a statistical study where the signal noise was systematically increased up to 40% is shown. In summary, the network is capable of handling trips of a maximum of 5000 steps and a noise level of 20% before the insect cannot find its way back. These results are on a par with those presented by Stone et al.<sup>34</sup> and represent a clear success of the network with the III–V components.

**Operational Efficiencies of the III–V Nanowire-Network Implementation.** In each step of transmission, detection, and signal processing in the network circuit, energy is dissipated, either due to conversion losses or intensity leaking out of the waveguide. To counteract the power dissipation and achieve stable operation, enough built-in signal amplification is required in the output of each neural node to drive the subsequent input in other nodes (fulfilling demands on fan-out and cascability<sup>41</sup>). We discuss the different efficiencies in the process, evaluate their magnitudes based on our calculations and experimental values to demonstrate the feasibility of our approach, and estimate necessary efficiency demands.

Starting from the optical input signals in the III–V neural node component, the photon-exciton conversion efficiency (antenna efficiency  $\eta_a$ ) describes how efficiently the photons absorbed in the components generate electron–hole pairs in the base and collector regions of the two npn phototransistors. The efficiency of converting the electronic signal back to photons in the LED branch (the internal quantum efficiency (IQE),  $\eta_{\text{IQE}}$ ) describes the relative effectiveness of the radiative recombination compared to competing processes, such as trap-

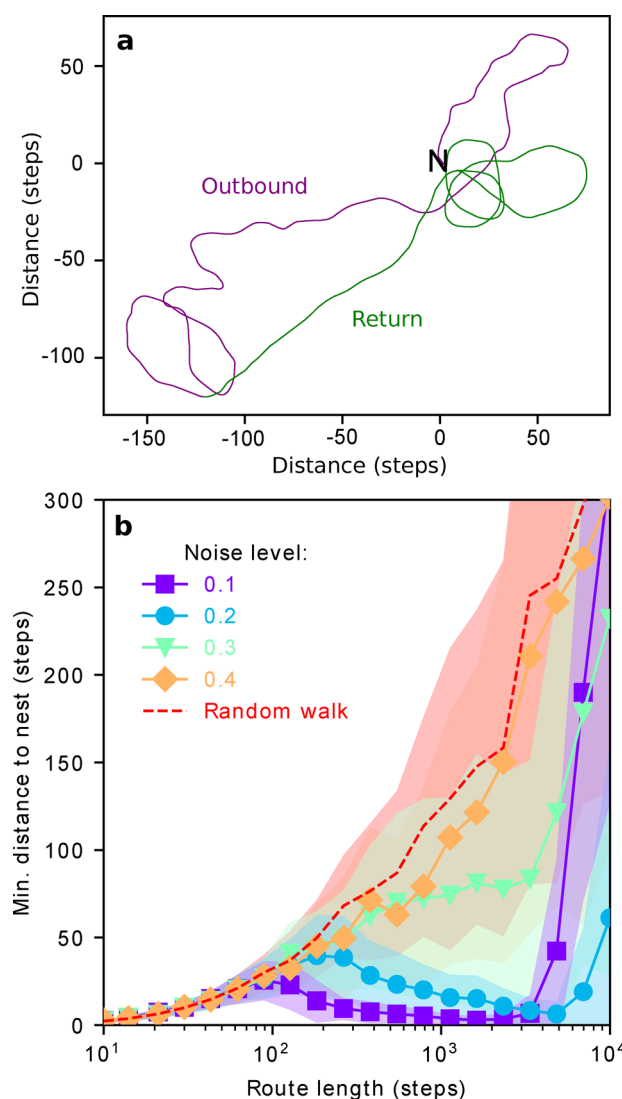


**Figure 6.** Simulated navigation using the model of Stone et al.<sup>34</sup> implemented with the specific III–V network circuit proposed here. (a) An example insect travel route obtained by the full navigation computational model with the results of the simulated III–V nanowire-based network integrated. First, the insect performs a random foraging trip (purple line). At a given point, it is switched to return home to the nest, indicated by N (green line). When it reaches the nest, it will keep circling it, as seen in the green line trace. (b) Statistics of the success rate for 1000 traveled routes distributed on 20 different trip lengths for different noise levels. The standard deviation is depicted as filled areas around the respective lines. For comparison, a reference case using a random walk for homing is also shown.

assisted recombination and Auger recombination. Then the light extraction efficiency  $\eta_{\text{out}}$  multiplies with the IQE to provide the external quantum efficiency of the LED. To compensate for the power lost in these processes, each node is required to have a gain mechanism so that it can generate the output needed to stimulate the subsequent components. In our approach, this is the current gain  $\beta_{\pm}$  of the excitation and inhibition transistor, respectively.

Approximating these parameters to be the same for all nanowire nodes, for the sake of this estimate, the output power of component (i) in terms of absorbed power, process efficiencies, and amplification then reads:



$$P_{\text{out},i} = \beta \eta_{\text{out}} \eta_{\text{IQE}} \eta_{\text{a}} P_{\text{abs},i}$$

The absorbed power ( $P_{\text{abs},i}$ ) consists of contributions from all other node components as well as exterior (compass) input. For a given node ( $i$ ), the power contribution from node ( $j$ ) can be calculated using the geometrical coupling coefficient  $g_{ij}(r)$ , describing the overlap of the emission light pattern of ( $j$ ) and the absorption cross-section of ( $i$ ). For cascability and fan-out to be fulfilled, a node must be able to deliver at least  $P_{\text{abs}}$  to the other nodes in order to activate them. Demanding that node ( $j$ ) must be able to supply the full power needed for node ( $i$ ) constitutes an upper limit of power needed, so

$$g_{ij} P_{\text{out},j} \geq P_{\text{abs},i}$$

Finally, noting that all neural node components are identical (the output powers of ( $i$ ) and ( $j$ ) will be similar in size) leads to the inequality:

$$g_{ij} \eta_{\text{out}} \eta_{\text{IQE}} \eta_{\text{a}} \geq \frac{1}{\beta}$$

which relate the losses and efficiencies to the current gain of the npn bipolar phototransistors. Most of the values in this equation can be determined from the modeling and experimentally known values. For the ring attractor, the strongest geometrical coupling coefficient is  $g_{ij} \approx 0.006$  (as shown in Figure 5c). This includes the waveguide loss and describes how much of the total signal reaches a connected component with the largest weighting factor. The internal quantum efficiency is closely related to the trap-assisted recombination lifetime of 1.34 ns used here for the III–V nanowires.<sup>42</sup> From the node component modeling (further detailed in the SI), a maximum efficiency of  $\eta_{\text{IQE}} = 0.7$  for a current density of  $J = 800 \text{ A/cm}^2$  was found. This number is well beyond the low-current limit for npn bipolar phototransistors where  $\beta$  saturates.<sup>43</sup> Regarding the antenna efficiency, it has been shown recently that InP nanowires with a diameter of 310 nm, designed for solar cells, enjoy a photocarrier collection efficiency of 90% over several microns.<sup>44</sup> The diameter is similar to the one used in the present work, which motivates the choice of  $\eta_{\text{a}} = 0.9$ . As a final step the current gain factor was set to  $\beta = 1900$  based on the component modeling results. This leads us to an estimate for the required light extraction efficiency from the LED

$$\eta_{\text{out}} > \frac{1}{g_{ij} \eta_{\text{IQE}} \eta_{\text{a}}} \frac{1}{\beta} \approx 0.14$$

This is well below the number of 42%, as reported by Reimer et al.,<sup>19</sup> demonstrating that the proposed network circuit appears feasible given realistic values from experiments and modeling. However, as discussed below, further work will be important for improving the energy efficiency of the system.

## DISCUSSION

We have proposed and successfully simulated an optoelectronic design to implement the nodes and connections of a neural circuit, closely based on the insect brain, that carries out an important navigational task. A relevant question is if all components are available for a practical realization of the proposed implementation. III–V nanopillar bipolar phototransistors have been developed, exhibiting transistor gain at subpicowatt levels.<sup>45</sup> Nanowire-based optical emitters that can perform above the required efficiencies have been exper-

imentally realized.<sup>19,20</sup> Electrically pumped sources with high efficiency have been reported in the III–V material system as well.<sup>46</sup> Individual nanowires have been demonstrated<sup>23</sup> to have a light concentration factor of 8 and high efficiency nanowire solar cells have been realized.<sup>22</sup>

The subcomponents of phototransistors and LED are most elegantly connected in a T-shaped or crossed nanowire structure. Branched III–V nanowires have been grown by several groups with a large level of control using catalyst migration.<sup>47,48</sup> Crossing nanowires in the III–V material system have been grown epitaxially by placing two growth substrates at an angle toward each other with the nanowires meeting and crossing during growth.<sup>49</sup> Other nanocrosses have been grown from both a hexagonal and cubic basis.<sup>50</sup> As an alternative implementation, two wires positioned in close proximity and connected with a metal bond could perform the same tasks.

A network that requires many nodes with similar operating parameters is a challenge to realize in most nanotechnologies. However, the present analog computational circuit has a large robustness built into the architecture. This is demonstrated by the statistical outcome of the navigation tests that was performed on the network (shown in Figure 6). A signal noise of 20% can be tolerated before the results become significantly worse than the noise-free reference. In addition, the effect of inaccuracy of the positioning of each node component is estimated in the Methods section, addressing the deviations in rotational alignment precision of the individual nodes. Deviations of up to 13° can be tolerated for the largest coupling coefficient. This indicates that significant variations in component positioning and perfection can be tolerated. For the necessary optimization, a wide variety of microscopy-based diagnostic tools are available for optimization of the optical fields and electron excitation locally in III–V nanowire structures.<sup>51,52</sup>

The LED polarization engineering is not a major obstacle to constructing the components. InP nanowires have a giant polarization anisotropy,<sup>37</sup> which naturally helps shape the optimal emission pattern shown in Figure 5b. Embedding the nanowire components in a waveguide decreases the dielectric contrast and reduces the anisotropy. To re-enhance this anisotropy, one option is to use a tapered nanowire cavity,<sup>19</sup> which has the additional benefit that it, through the Purcell effect, decreases the spontaneous emission lifetime in the quantum dot. This directly leads to a better efficiency  $\eta_{\text{IQE}}$  of the LED, which translates to lower operating currents and power consumption. Better emission control also allows a decrease in the network diameter and thus increases the geometrical coupling coefficients  $g_{ij}$ . Among other possible improvements,<sup>53</sup> the antenna structure demonstrated by Ramezani et al.<sup>54</sup> is suitable for controlling the emission from the nanowire LED.

The shared waveguide design dispenses with intercomponent wiring or waveguides and instead allows setting the weights using the geometry of the system. This strategy enables a small footprint and low energy use. Further generalizing this concept to different networks might require additional design developments and new light focusing components. However, a wide variety of subwavelength nanophotonic structures have been designed recently that can guide light to focus at specified points with varying intensity. Wiring to supply power to the active components is still required, and this will cause some additional scattering. Indium tin oxide (ITO) is a transparent

conductor at the wavelengths of interest with a refractive index (2.1) close to that of  $\text{HfO}_2$  (1.8) and can thus be used to minimize this scattering. Although imperfections in the deposition are likely to occur, this is not foreseen as a major obstacle.

Before finally discussing the power consumption of our network solution, we would like to put it in context by briefly relating it to biological systems and CMOS technology. The human brain is known to require 10–20 W of power. Based on simple assumptions the energy consumption per neuron and operation has been estimated<sup>1</sup> at  $10^{-16}$  J. More detailed studies of the energy consumption of the neural system in the brain have been put forward, however, estimates end up in a similar range.<sup>55</sup> Exactly how the brain spends this energy is a matter of debate, but it has been estimated that around 70% is used for interneuron communication.<sup>56</sup> Using CMOS solutions particularly optimized toward neural networks, efficiencies in the range of  $10^{-11}$  J per operation have been achieved.<sup>2,57</sup> This is already considerably better than standard computers, but orders of magnitude below the efficiency of the human brain.

The power dissipation bottleneck in the present design is the nanowire LED efficiency. In order for the total losses not to overcome the transistor gain factor, the LED must be operated at a relatively high external quantum efficiency. As an example, a moderate internal efficiency of 50% requires a current through the LED of about  $100 \text{ A/cm}^2$ . This corresponds to  $\sim 2 \text{ nA}$  in the branch. Assuming that a few volts is applied to the component and that there is additional energy dissipation due to possible inhibition, a power use of  $\sim 10 \text{ nW}$  per neural node component during operation can be estimated. The energy needed per operation depends on the frequency, but with experimentally verified values for components and reasonable assumptions on operation, an energy dissipation of  $10^{-16}$  J/operation or less can be reached (see the SI for more details), equivalent to the levels observed in biological brains. To further reduce the power consumption, the most important optimization is the LED efficiency at lower currents. If the trap-recombination lifetimes could be increased toward bulk values of InP, an improvement of 1 or 2 orders of magnitude can be expected.

## CONCLUSIONS

Two major new concepts for an artificial neural network system based on nanoscale optoelectronics have been investigated. First, optical communication is done directly via broadcasting, with all components in the same 2D slab confining the radiation. This radically reduces the footprint of the neural network since no wiring (electrical or fiber) between components is needed. Second, a mature III–V nanowire technology platform is used to create the neural nodes. The nanowires have light absorption cross sections much larger than their geometric dimensions and the III–V materials are very efficient in photon–electron conversion. To investigate their feasibility, these concepts were implemented on the most heavily interconnected part of a specific, anatomically verified model of the navigation center of the insect brain. This allowed a thorough simulation of all electrical and optical parts of the network using experimentally verified parameters. Using conservative estimates for all parameters and already available nanowire technology, the network is shown to function and can be orders of magnitude more efficient than present technologies.

While the present work can be viewed as a proof of principle, it also identifies challenges for the development of such networks in terms of component design. Central is the power efficiency of the artificial neuron. The more efficient emission and absorption of light in the nanowire components, the more favorable solutions become. Another important challenge is the placement of the components and the focusing of light in subwavelength structures. For placement, technology relevant for other applications such as III–V nanowire-based quantum computers face similar challenges, and several solutions have been put forward. The focusing and manipulation of light on a subwavelength scale have seen a wealth of new developments in recent years, thus, it would even be possible to create advanced patterns that can act as low footprint communication paths. Again, energy dissipation is an important issue as many such components have significant losses.

The ring-attractor system implemented is, in principle, dedicated to a specific navigational task. Importantly, its functional connectivity can be expressed in geometrical terms that exploit a light broadcast as a method of internode communication. The extent to which this may be a general principle in biological neural networks is unknown, but the ring attractor itself appears to subserve a wide range of navigational functions for the insect. As such, the methodology described might have the greatest application for reproducing specific, but crucial, capabilities of biological brains. On the other hand, the proposed nanoscale nonlinear processing unit with optical input and output may serve as the minimal unit in many other neural network approaches.

## METHODS

**Electronic Modeling of the Node Component.** A detailed account of the node component modeling is given in the SI, but a short summary is provided here. A drift-diffusion model with thermionic emission boundary conditions was implemented in COMSOL to calculate the transport in the nanowire subcomponents. Similar models have been shown to yield good agreement with experimental data for InAs nanowire heterostructures<sup>58</sup> and InP *pn*-junctions.<sup>59</sup> The components studied here are heavily doped, and the main effect due to the surface is the increased carrier recombination due to surface states, which is why no explicit surface charge was considered here. An effective 1D model was used where the surface recombination term enters as an additional trap-assisted recombination process.<sup>60</sup> The modeling was divided into two steps. In the first, the two nanowire npn phototransistors and the LED were modeled. The results were fitted to an Ebers-Moll model and the Shockley diode equation, respectively. In the second step, these were used as elements in the equivalent circuit of our node component, as shown in Figure 2b. Here the two current sources  $I_-$  and  $I_+$  represent the photoinduced current in the base and collector regions of the respective transistors. To provide a saturation level to the output of the nanowire-based nodes, a large external resistance  $R_{\text{load}}$  is used. The resulting load line imposes an approximate maximum current level on the circuit for the range of biases used. Using a spice solver, the final results are extracted as shown in Figure 3b.

This trapping of holes increases the optical gain of the npn phototransistors.<sup>36</sup> However, the fast trap and surface recombination in nanowires strongly limits the gain and the functionality. This study used a realistic electron and hole recombination lifetime of 1.34 ns, as measured at room

temperature,<sup>42</sup> together with the experimentally observed mobilities.<sup>42</sup> Despite these limitations, nanowire npn phototransistors can deliver current gain  $\beta > 1900$ , which is needed to transmit the signals across the ring attractor.

For the nanowire LED, the fast recombination process prevents a high efficiency at low currents, as a large current density is needed for the spontaneous emission process to compete with nonradiative processes. In this work, the momentum matrix element for the spontaneous emission process is calculated from the Kane energy of InP of 20.7 eV.<sup>61</sup>

In order to use the simulated activation function in the computational model, the output current through the LED was normalized by the saturation current  $I_{\text{sat}}$ , while the input currents were normalized instead by  $I_{\text{sat}}/\beta_-$  to take the amplification in each npn phototransistor into account. This directly yields the activation function shown as a dashed line in the ring attractor inset of Figure 3b.

**Optical Modeling of the Network.** In the FDTD 3D model, the ring attractor network of 8 components was placed inside a guiding layer of 300 nm  $\text{HfO}_2$ , surrounded by  $\text{SiO}_2$  and air, as shown in Figure 4a,b. This quasi-2D waveguide confines 60% of the intensity emitted by the components inside the network, which would otherwise suffer dramatic losses. It has been designed for a wavelength of 830 nm, which matches the bandgap of InP used for the absorbing region of the inhibition transistor (red in Figure 2a) and for the recombination region of the nanowire LED. A dipole source, representing the nanowire LED, was placed 100 nm from the end of the nanowire branch in node 3, oriented along the branch axis. The network circumference, with respect to the center of gravity of the nanowire stem of each component, was set to

$$2\pi R_{\text{network}} = 2L_{\text{branch}}N_{\text{nodes}}$$

in order to leave generous space between components for wiring. This resulted in a network of diameter  $2R_{\text{network}} = 5.1 \mu\text{m}$ . The InP and  $\text{SiO}_2$  was modeled using the data of Palik,<sup>62</sup> the  $\text{HfO}_2$  using Wood et al.,<sup>63</sup> while the wide-gap material  $\text{Al}_{0.3}\text{In}_{0.7}\text{P}$  was modeled as a dielectric with refractive index  $n(\text{AlInP}) = 3.3$ , as its dispersive properties are of little interest in this study.

Nominally, each component was positioned with the nanowire stem directed toward the center. However, in order to enhance the opposite coupling coefficient (e.g.,  $g_{15}$ ) and to reduce the coupling to the clockwise neighbor (e.g.,  $g_{12}$ ), each component was subsequently rotated 0.3 rad in the clockwise direction around the waveguide normal, as seen in Figure 4a, still keeping the normal orientation of the nanowire branch relative to the nanowire stem. It is possible to estimate the effect of positioning noise relative to this rotation. If the allowed reduction of the strongest weight  $g_{15}$  is denoted  $p$ , we find the maximum tolerable angle from expanding the power of the ideal dipolar radiation pattern  $\cos^2\theta$  around  $\theta = 0$ , as

$$1 - p = \cos^2(\theta) \approx (1 - \theta^2/2)^2 \approx 1 - \theta^2$$

which provides  $(\Delta\theta)^2 = \Delta p$ . It has been shown that the CX can navigate successfully with 5% weight noise.<sup>34</sup> Using  $p = 0.05$ , we find a corresponding uncertainty in angle of  $\Delta\theta = 13^\circ$ , which indicates that some noise in the positioning of the components is tolerable. Expansions far from the peak are less favorable, giving a smaller allowed uncertainty for coupling coefficients of components closer to each other. However, the

absolute value of these coefficients is smaller in general, which limits the impact of positioning errors in these couplings.

**Modeling of the Complete Navigation System.** The complete network has been implemented in Python 2.7, as described previously.<sup>34</sup> The three layers of the neural circuit depicted in Figure 1 (lower right inset) have nodes with activation functions tuned for a specific functionality. In the present work, the program was modified to take the weights and neural performance of the III–V components solution into account. The two-variable activation function was interpolated by the program from a given discrete 2D map (see SI). The weights were given as a matrix. In order to test the robustness of the computational capability of the circuit, the simulations feature different levels of noise. The noise is added to the result processed by each activation function (final value clipped to the interval  $[0,1]$ ), both inside and outside the ring attractor. This number corresponds to the amplitude of the white noise that was added to the signal, which was in turn normalized to unity.

## ■ ASSOCIATED CONTENT

### SI Supporting Information

The Supporting Information is available free of charge at <https://pubs.acs.org/doi/10.1021/acsphotonics.0c01003>.

A detailed material model is presented supporting both the electronic and optical simulations of the semiconductor components. Extensive modeling results for the neural node subcomponents as well as for the combined component are shown, including methods for tuning the slope and saturation current. The final circuit is analyzed in terms of energy cost per operation, at low and high operation frequencies. In addition, simulations of dipole emission in all directions relative to the nanowire branch are presented, and the resulting weight matrix is used as input to the full navigational circuit (PDF)

## ■ AUTHOR INFORMATION

### Corresponding Authors

**David O. Winge** – Department of Physics and NanoLund, Lund University, 221 00 Lund, Sweden; [orcid.org/0000-0001-5191-9728](https://orcid.org/0000-0001-5191-9728); Email: [david.winge@sljus.lu.se](mailto:david.winge@sljus.lu.se)

**Anders Mikkelsen** – Department of Physics and NanoLund, Lund University, 221 00 Lund, Sweden; Email: [anders.mikkelsen@sljus.lu.se](mailto:anders.mikkelsen@sljus.lu.se)

### Authors

**Steven Limpert** – Department of Physics and NanoLund, Lund University, 221 00 Lund, Sweden

**Heiner Linke** – Department of Physics and NanoLund, Lund University, 221 00 Lund, Sweden; [orcid.org/0000-0003-4451-4006](https://orcid.org/0000-0003-4451-4006)

**Magnus T. Borgström** – Department of Physics and NanoLund, Lund University, 221 00 Lund, Sweden; [orcid.org/0000-0001-8061-0746](https://orcid.org/0000-0001-8061-0746)

**Barbara Webb** – School of Informatics, University of Edinburgh, Edinburgh EH8 9AB, United Kingdom

**Stanley Heinze** – Lund Vision Group, Department of Biology, Lund University, 22362 Lund, Sweden

Complete contact information is available at:

<https://pubs.acs.org/doi/10.1021/acsphotonics.0c01003>



## Author Contributions

A.M. conceived the project and initiated the work. A.M. and D.O.W. designed the component and the network with important input from S.L., H.L., M.T.B., B.W., and S.H. D.O.W. performed the simulations, analyzed the data, optimized the component and network, and prepared the figures. A.M. and D.O.W. wrote the manuscript with significant contributions from all other authors. All authors engaged in discussions and analysis of the results.

## Notes

The authors declare no competing financial interest.

## ACKNOWLEDGMENTS

This work was supported by the Swedish Research Council (VR) and NanoLund FutureThemes. S.H. was supported by the European Research Council (ERC) under the European Union's Horizon 2020 research and innovation program (Grant Agreement No. 714599). D.O.W. and A.M. were supported by the Office of Naval Research (Grant No. N62909-20-1-2038).

## REFERENCES

- (1) Mead, C. Neuromorphic Electronic Systems. *Proc. IEEE* **1990**, 78 (10), 1629–1636.
- (2) Merolla, P. A.; Arthur, J. V.; Alvarez-Icaza, R.; Cassidy, A. S.; Sawada, J.; Akopyan, F.; Jackson, B. L.; Imam, N.; Guo, C.; Nakamura, Y.; Brezzo, B.; Vo, I.; Esser, S. K.; Appuswamy, R.; Taba, B.; Amir, A.; Flickner, M. D.; Risk, W. P.; Manohar, R.; Modha, D. S. A Million Spiking-Neuron Integrated Circuit with a Scalable Communication Network and Interface. *Science* **2014**, 345 (6197), 668–673.
- (3) Wang, Z.; Joshi, S.; Savel'Ev, S.; Song, W.; Midya, R.; Li, Y.; Rao, M.; Yan, P.; Asapu, S.; Zhuo, Y.; Jiang, H.; Lin, P.; Li, C.; Yoon, J. H.; Upadhyay, N. K.; Zhang, J.; Hu, M.; Strachan, J. P.; Barnell, M.; Wu, Q.; Wu, H.; Williams, R. S.; Xia, Q.; Yang, J. J. Fully Memristive Neural Networks for Pattern Classification with Unsupervised Learning. *Nat. Electron.* **2018**, 1 (2), 137–145.
- (4) Fuller, E. J.; Gabaly, F. El; Léonard, F.; Agarwal, S.; Plimpton, S. J.; Jacobs-Gedrim, R. B.; James, C. D.; Marinella, M. J.; Talin, A. A. Li-Ion Synaptic Transistor for Low Power Analog Computing. *Adv. Mater.* **2017**, 29 (4), 1604310.
- (5) Locatelli, N.; Cros, V.; Grollier, J. Spin-Torque Building Blocks. *Nat. Mater.* **2014**, 13 (1), 11–20.
- (6) Tanaka, G.; Yamane, T.; Héroux, J. B.; Nakane, R.; Kanazawa, N.; Takeda, S.; Numata, H.; Nakano, D.; Hirose, A. Recent Advances in Physical Reservoir Computing: A Review. *Neural Networks* **2019**, 115, 100–123.
- (7) Ferreira de Lima, T.; Shastri, B. J.; Tait, A. N.; Nahmias, M. A.; Prucnal, P. R. Progress in Neuromorphic Photonics. *Nanophotonics* **2017**, 6 (3), 577–599.
- (8) Van Der Sande, G.; Brunner, D.; Soriano, M. C. Advances in Photonic Reservoir Computing. *Nanophotonics* **2017**, 6 (3), 561–576.
- (9) Zhang, Q.; Yu, H.; Barbiero, M.; Wang, B.; Gu, M. Artificial Neural Networks Enabled by Nanophotonics. *Light: Sci. Appl.* **2019**, 8 (1), 42.
- (10) Shen, Y.; Harris, N. C.; Skirlo, S.; Prabhu, M.; Baehr-Jones, T.; Hochberg, M.; Sun, X.; Zhao, S.; Larochelle, H.; Englund, D.; Soljačić, M. Deep Learning with Coherent Nanophotonic Circuits. *Nat. Photonics* **2017**, 11 (7), 441–446.
- (11) Larger, L.; Baylón-Fuentes, A.; Martinenghi, R.; Udaltsov, V. S.; Chembo, Y. K.; Jacquot, M. High-Speed Photonic Reservoir Computing Using a Time-Delay-Based Architecture: Million Words per Second Classification. *Phys. Rev. X* **2017**, 7 (1), 1–14.
- (12) Tait, A. N.; De Lima, T. F.; Zhou, E.; Wu, A. X.; Nahmias, M. A.; Shastri, B. J.; Prucnal, P. R. Neuromorphic Photonic Networks Using Silicon Photonic Weight Banks. *Sci. Rep.* **2017**, 7 (1), 7430.
- (13) Shainline, J. M.; Buckley, S. M.; Mirin, R. P.; Nam, S. W. Superconducting Optoelectronic Circuits for Neuromorphic Computing. *Phys. Rev. Appl.* **2017**, 7 (3), 034013.
- (14) Prucnal, P. R.; Shastri, B. J.; Teich, M. C. *Neuromorphic Photonics*; Prucnal, P. R., Shastri, B. J., Eds.; CRC Press, 2017.
- (15) Garnett, E. C.; Brongersma, M. L.; Cui, Y.; McGehee, M. D. Nanowire Solar Cells. *Annu. Rev. Mater. Res.* **2011**, 41 (1), 269–295.
- (16) van Dam, D.; van Hoof, N. J. J.; Cui, Y.; van Veldhoven, P. J.; Bakkers, E. P. A. M.; Gómez Rivas, J.; Haverkort, J. E. M. High-Efficiency Nanowire Solar Cells with Omnidirectionally Enhanced Absorption Due to Self-Aligned Indium–Tin–Oxide Mie Scatterers. *ACS Nano* **2016**, 10 (12), 11414–11419.
- (17) Otnes, G.; Borgström, M. T. Towards High Efficiency Nanowire Solar Cells. *Nano Today* **2017**, 12, 31–45.
- (18) Ra, Y.-H.; Rashid, R. T.; Liu, X.; Sadaf, S. M.; Mashooq, K.; Mi, Z. An Electrically Pumped Surface-Emitting Semiconductor Green Laser. *Sci. Adv.* **2020**, 6 (1), eaav7523.
- (19) Reimer, M. E.; Bulgarini, G.; Akopian, N.; Hocevar, M.; Bavinck, M. B.; Verheijen, M. A.; Bakkers, E. P. A. M.; Kouwenhoven, L. P.; Zwiller, V. Bright Single-Photon Sources in Bottom-up Tailored Nanowires. *Nat. Commun.* **2012**, 3 (1), 737.
- (20) Claudon, J.; Bleuse, J.; Malik, N. S.; Bazin, M.; Jaffrennou, P.; Gregersen, N.; Sauvan, C.; Lalanne, P.; Gérard, J. M. A Highly Efficient Single-Photon Source Based on a Quantum Dot in a Photonic Nanowire. *Nat. Photonics* **2010**, 4 (3), 174–177.
- (21) Li, K. H.; Liu, X.; Wang, Q.; Zhao, S.; Mi, Z. Ultralow-Threshold Electrically Injected AlGaIn Nanowire Ultraviolet Lasers on Si Operating at Low Temperature. *Nat. Nanotechnol.* **2015**, 10 (2), 140–144.
- (22) Wallentin, J.; Anttu, N.; Asoli, D.; Huffman, M.; Aberg, I.; Magnusson, M. H.; Siefer, G.; Fuss-Kailuweit, P.; Dimroth, F.; Witzigmann, B.; Xu, H. Q.; Samuelson, L.; Deppert, K.; Borgström, M. T. InP Nanowire Array Solar Cells Achieving 13.8% Efficiency by Exceeding the Ray Optics Limit. *Science* **2013**, 339 (6123), 1057–1060.
- (23) Krogstrup, P.; Jørgensen, H. I.; Heiss, M.; Demichel, O.; Holm, J. V.; Aagesen, M.; Nygard, J.; Fontcuberta I Morral, A. Single-Nanowire Solar Cells beyond the Shockley-Queisser Limit. *Nat. Photonics* **2013**, 7 (4), 306–310.
- (24) Cao, L.; White, J. S.; Park, J. S.; Schuller, J. A.; Clemens, B. M.; Brongersma, M. L. Engineering Light Absorption in Semiconductor Nanowire Devices. *Nat. Mater.* **2009**, 8 (8), 643–647.
- (25) Yang, H.; Khayrudinov, V.; Dhaka, V.; Jiang, H.; Autere, A.; Lipsanen, H.; Sun, Z.; Jussila, H. Nanowire Network-Based Multifunctional All-Optical Logic Gates. *Sci. Adv.* **2018**, 4 (7), eaar7954.
- (26) Yang, I.; Li, Z.; Wong-Leung, J.; Zhu, Y.; Li, Z.; Gagrani, N.; Li, L.; Lockrey, M. N.; Nguyen, H.; Lu, Y.; Tan, H. H.; Jagadish, C.; Fu, L. Multiwavelength Single Nanowire InGaAs/InP Quantum Well Light-Emitting Diodes. *Nano Lett.* **2019**, 19 (6), 3821–3829.
- (27) Borgström, M. T.; Zwiller, V.; Müller, E.; Imamoglu, A. Optically Bright Quantum Dots in Single Nanowires. *Nano Lett.* **2005**, 5 (7), 1439–1443.
- (28) Mantynen, H.; Anttu, N.; Sun, Z.; Lipsanen, H. Single-Photon Sources with Quantum Dots in III-V Nanowires. *Nanophotonics* **2019**, 8 (5), 747–769.
- (29) Warrant, E.; Frost, B.; Green, K.; Mouritsen, H.; Dreyer, D.; Adden, A.; Brauburger, K.; Heinze, S. The Australian Bogong Moth *Agrotis Infusa*: A Long-Distance Nocturnal Navigator. *Front. Behav. Neurosci.* **2016**, 10, 77.
- (30) Reppert, S. M.; de Roode, J. C. Demystifying Monarch Butterfly Migration. *Curr. Biol.* **2018**, 28, R1009–R1022.
- (31) Heinze, S.; Narendra, A.; Cheung, A. Principles of Insect Path Integration. *Curr. Biol.* **2018**, 28, R1043–R1058.
- (32) Honkanen, A.; Adden, A.; da Silva Freitas, J.; Heinze, S. The Insect Central Complex and the Neural Basis of Navigational Strategies. *J. Exp. Biol.* **2019**, 222, jeb188854.



- (33) Pfeiffer, K.; Homberg, U. Organization and Functional Roles of the Central Complex in the Insect Brain. *Annu. Rev. Entomol.* **2014**, *59* (1), 165–184.
- (34) Stone, T.; Webb, B.; Adden, A.; Weddig, N. B.; Honkanen, A.; Templin, R.; Wcislo, W.; Scimeca, L.; Warrant, E.; Heinze, S. An Anatomically Constrained Model for Path Integration in the Bee Brain. *Curr. Biol.* **2017**, *27* (20), 3069–3085.
- (35) Gramotnev, D. K.; Bozhevolnyi, S. I. Plasmonics beyond the Diffraction Limit. *Nat. Photonics* **2010**, *4* (2), 83–91.
- (36) Campbell, J. C.; Ogawa, K. Heterojunction Phototransistors for Long-Wavelength Optical Receivers. *J. Appl. Phys.* **1982**, *53* (2), 1203–1208.
- (37) Wang, J. Highly Polarized Photoluminescence and Photo-detection from Single Indium Phosphide Nanowires. *Science* **2001**, *293* (5534), 1455–1457.
- (38) Lumerical Inc. *FDTD Solutions*; Lumerical, 2018.
- (39) Holsteen, A. L.; Raza, S.; Fan, P.; Kik, P. G.; Brongersma, M. L. Purcell Effect for Active Tuning of Light Scattering from Semiconductor Optical Antennas. *Science* **2017**, *358* (6369), 1407–1410.
- (40) Bulgarini, G.; Dalacu, D.; Poole, P. J.; Lapointe, J.; Reimer, M. E.; Zwiller, V. Far Field Emission Profile of Pure Wurtzite InP Nanowires. *Appl. Phys. Lett.* **2014**, *105* (19), 191113.
- (41) Miller, D. A. B. Are Optical Transistors the Logical next Step? *Nat. Photonics* **2010**, *4* (1), 3–5.
- (42) Joyce, H. J.; Wong-Leung, J.; Yong, C. K.; Docherty, C. J.; Paiman, S.; Gao, Q.; Tan, H. H.; Jagadish, C.; Lloyd-Hughes, J.; Herz, L. M.; Johnston, M. B. Ultralow Surface Recombination Velocity in InP Nanowires Probed by Terahertz Spectroscopy. *Nano Lett.* **2012**, *12* (10), 5325–5330.
- (43) Fritzsche, D.; Kuphal, E.; Aulbach, R. Fast Response InP/InGaAsP Heterojunction Phototransistors. *Electron. Lett.* **1981**, *17* (5), 178–180.
- (44) Mann, S. A.; Oener, S. Z.; Cavalli, A.; Haverkort, J. E. M.; Bakkers, E. P. A. M.; Garnett, E. C. Quantifying Losses and Thermodynamic Limits in Nanophotonic Solar Cells. *Nat. Nanotechnol.* **2016**, *11* (12), 1071–1075.
- (45) Ko, W. S.; Bhattacharya, I.; Tran, T.-T. D.; Ng, K. W.; Adair Gerke, S.; Chang-Hasnain, C. Ultrahigh Responsivity-Bandwidth Product in a Compact InP Nanopillar Phototransistor Directly Grown on Silicon. *Sci. Rep.* **2016**, *6* (1), 33368.
- (46) Heindel, T.; Schneider, C.; Lermer, M.; Kwon, S. H.; Braun, T.; Reitzenstein, S.; Höfling, S.; Kamp, M.; Forchel, A. Electrically Driven Quantum Dot-Micropillar Single Photon Source with 34% Overall Efficiency. *Appl. Phys. Lett.* **2010**, *96* (1), 2008–2011.
- (47) Tornberg, M.; Dick, K. A.; Lehmann, S. Branched InAs Nanowire Growth by Droplet Confinement. *Appl. Phys. Lett.* **2018**, *113* (12), 123104.
- (48) Kelrich, A.; Sorias, O.; Calahorra, Y.; Kauffmann, Y.; Gladstone, R.; Cohen, S.; Orenstein, M.; Ritter, D. InP Nanoflag Growth from a Nanowire Template by in Situ Catalyst Manipulation. *Nano Lett.* **2016**, *16* (4), 2837–2844.
- (49) Plissard, S. R.; Van Weperen, I.; Car, D.; Verheijen, M. A.; Immink, G. W. G.; Kammhuber, J.; Cornelissen, L. J.; Szombati, D. B.; Geresdi, A.; Frolov, S. M.; Kouwenhoven, L. P.; Bakkers, E. P. A. M. Formation and Electronic Properties of InSb Nanocrosses. *Nat. Nanotechnol.* **2013**, *8* (11), 859–864.
- (50) Krizek, F.; Kanne, T.; Razmadze, D.; Johnson, E.; Nygård, J.; Marcus, C. M.; Krogstrup, P. Growth of InAs Wurtzite Nanocrosses from Hexagonal and Cubic Basis. *Nano Lett.* **2017**, *17* (10), 6090–6096.
- (51) Zakharov, A. A.; Mikkelsen, A.; Andersen, J. N. Recent Advances in Imaging of Properties and Growth of Low Dimensional Structures for Photonics and Electronics by XPEEM. *J. Electron Spectrosc. Relat. Phenom.* **2012**, *185* (10), 417–428.
- (52) Mårsell, E.; Boström, E.; Harth, A.; Losquin, A.; Guo, C.; Cheng, Y.-C.; Lorek, E.; Lehmann, S.; Nylund, G.; Stankovski, M.; Arnold, C. L.; Miranda, M.; Dick, K. A.; Mauritsson, J.; Verdozzi, C.; L'Huillier, A.; Mikkelsen, A. Spatial Control of Multiphoton Electron Excitations in InAs Nanowires by Varying Crystal Phase and Light Polarization. *Nano Lett.* **2018**, *18* (2), 907–915.
- (53) Koenderink, A. F. Single-Photon Nanoantennas. *ACS Photonics* **2017**, *4* (4), 710–722.
- (54) Ramezani, M.; Casadei, A.; Grzela, G.; Matteini, F.; Tütüncüoğlu, G.; Ruffer, D.; Fontcuberta i Morral, A.; Gómez Rivas, J. Hybrid Semiconductor Nanowire-Metallic Yagi-Uda Antennas. *Nano Lett.* **2015**, *15* (8), 4889–4895.
- (55) Saxena, V.; Wu, X.; Srivastava, I.; Zhu, K. Towards Neuromorphic Learning Machines Using Emerging Memory Devices with Brain-like Energy Efficiency. *J. Low Power Electron. Appl.* **2018**, *8* (4), 34.
- (56) Tomasi, D.; Wang, G. J.; Volkow, N. D. Energetic Cost of Brain Functional Connectivity. *Proc. Natl. Acad. Sci. U. S. A.* **2013**, *110* (33), 13642–13647.
- (57) Wu, X.; Saxena, V.; Zhu, K.; Balagopal, S. A CMOS Spiking Neuron for Brain-Inspired Neural Networks with Resistive Synapses and in Situ Learning. *IEEE Trans. Circuits Syst. II Express Briefs* **2015**, *62* (11), 1088–1092.
- (58) Chen, I. J.; Lehmann, S.; Nilsson, M.; Kivisaari, P.; Linke, H.; Dick, K. A.; Thelander, C. Conduction Band Offset and Polarization Effects in InAs Nanowire Polytype Junctions. *Nano Lett.* **2017**, *17* (2), 902–908.
- (59) Chayanun, L.; Otnes, G.; Troian, A.; Hammarberg, S.; Salomon, D.; Borgström, M. T.; Wallentin, J. Nanoscale Mapping of Carrier Collection in Single Nanowire Solar Cells Using X-Ray Beam Induced Current. *J. Synchrotron Radiat.* **2019**, *26* (1), 102–108.
- (60) Chen, Y.; Kivisaari, P.; Pistol, M. E.; Anttu, N. Optimized Efficiency in InP Nanowire Solar Cells with Accurate 1D Analysis. *Nanotechnology* **2018**, *29* (4), 045401.
- (61) Vurgaftman, I.; Meyer, J. R.; Ram-Mohan, L. R. Band Parameters for III-V Compound Semiconductors and Their Alloys. *J. Appl. Phys.* **2001**, *89* (11), 5815–5875.
- (62) Palik, E. *Handbook of Optical Constants of Solids*; Academic Press, Elsevier Inc., 1991.
- (63) Wood, D. L.; Nassau, K.; Kometani, T. Y.; Nash, D. L. Optical Properties of Cubic Hafnia Stabilized with Yttria. *Appl. Opt.* **1990**, *29* (4), 604–607.